Dust and Cold Gas Properties of Starburst HyLIRG Quasars at z □ 2.5

(article starts on next page)

Dust and Cold Gas Properties of Starburst HyLIRG Quasars at $z \sim 2.5$

Feng-Yuan Liu[1,2,3] , Y. Sophia Dai[1] , Alain Omont[4] , Daizhong Liu[5] , Pierre Cox[4] , Roberto Neri[6] , Melanie Krips[6],
Chentao Yang[7] , Xue-Bing Wu[8,9] , and Jia-Sheng Huang[1,10]

[1] Chinese Academy of Sciences South America Center for Astronomy (CASSACA), National Astronomical Observatories (NAOC), 20A Datun Road, Beijing 100012, People's Republic of China; ydai@nao.cas.cn
[2] School of Astronomy and Space Science, University of Chinese Academy of Sciences, Beijing 101408, People's Republic of China
[3] Institute for Astronomy, University of Edinburgh, Royal Observatory, Edinburgh, EH9 3HJ, UK
[4] Sorbonne Université, UPMC Universit Paris 6 and CNRS, UMR 7095, Institut dAstrophysique de Paris, France
[5] Max-Planck-Institut für Extraterrestrische Physik (MPE), Giessenbachstr. 1, D-85748 Garching, Germany
[6] Institut de Radioastronomie Millimtrique (IRAM), 300 Rue de la Piscine, 38400 Saint-Martin–d'Héres, France
[7] Department of Space, Earth and Environment, Chalmers University of Technology, Onsala Space Observatory, 439 92 Onsala, Sweden
[8] Department of Astronomy, School of Physics, Peking University, Beijing 100871, People's Republic of China
[9] Kavli Institute for Astronomy and Astrophysics, Peking University, Beijing 100871, People's Republic of China
[10] Harvard-Smithsonian Center for Astrophysics, 60 Garden Street, Cambridge, MA 02215, USA

Abstract

Some high-z active galactic nuclei (AGNs) are found to reside in extreme star-forming galaxies, such as hyperluminous infrared galaxies (HyLIRGs), with AGN-removed L_{IR} of $>10^{13} L_\odot$. In this paper, we report NOEMA observations of six apparent starburst HyLIRGs associated with optical quasars at $z \sim 2$–3 in the Stripe 82 field, to study their dust and molecular CO properties. Five out of the six candidates are detected with CO(4–3) or CO(5–4) emission, and four in the 2 mm dust continuum. Based on the linewidth–$L'_{CO(1-0)}$ diagnostics, we find that four galaxies are likely unlensed or weakly lensed sources. The molecular gas mass is in the range of $\mu M_{H_2} \sim 0.8$–$9.7 \times 10^{10} M_\odot$ (with $\alpha = 0.8 M_\odot (K\ km\ s^{-1}\ pc^2)^{-1}$, where μ is the unknown possible gravitational magnification factor). We fit their spectral energy distributions, after including the observed 2 mm fluxes and upper limits, and estimate their apparent (uncorrected for possible lensing effects) star formation rates (μSFRs) to be $\sim$400–2500 $M_\odot\ yr^{-1}$, with a depletion time of $\sim$20–110 Myr. We notice interesting offsets, of $\sim$10–40 kpc spatially or $\sim$1000–2000 km s^{-1} spectroscopically, between the optical quasar and the millimeter continuum or CO emissions. The observed velocity shift is likely related to the blueshifted broad-emission-line region of quasars, though mergers or recoiling black holes are also possible causes, which can explain the spatial offsets and the high intrinsic star formation rates in the HyLIRG quasar systems.

Unified Astronomy Thesaurus concepts: Starburst galaxies (1570); CO line emission (262); Millimeter-wave spectroscopy (2252); Interferometry (808); Quasars (1319); Galaxy evolution (594)

1. Introduction

Active galactic nuclei (AGNs) represent a crucial phase in the evolution of supermassive black holes and may strongly influence the evolution of their host galaxies (Fabian 2012; Kormendy & Ho 2013). Observations have shown that the powerful phases of AGNs, i.e., quasars, influence host galaxies through either radiation pressure (e.g., Laor & Draine 1993; Scoville & Norman 1995) or AGN wind (e.g., Weymann et al. 1991; Pounds et al. 2003; Tombesi et al. 2012) during the so-called "quasar mode" feedback. This is consistent with the evolutionary model of quasars by Sanders et al. (1988), where quasars develop from dusty ultraluminous infrared galaxies (ULIRGs) with infrared (IR) luminosity $L_{IR} > 10^{12} L_\odot$. As the AGN feedback sweeps the gas and dust in the core region, the central AGN gets exposed in the line of sight and appears to be a type I broad-emission-line quasar. The star formation (SF) in the host galaxy is suppressed during the process.

This model indicates a transitional stage in quasar evolution, where a quasar coexists with a large amount of IR-luminous galactic dust. In observations, there are 10%–30% quasars with bright submillimeter/far-IR (FIR) excesses (e.g., Dai et al. 2012, 2018; Ma & Yan 2015; Dong & Wu 2016). Some of them have the most IR-luminous host galaxies, i.e., starburst hyperluminous infrared galaxies (HyLIRGs) with starburst-dominated $L_{IR} > 10^{13} L_\odot$. With an IR-traced SF rate (SFR) of $\gtrsim 10^3 M_\odot\ yr^{-1}$ (e.g., Casey et al. 2012; Banerji et al. 2013; Ivison et al. 2013), they link the most powerful AGNs and the most extreme SF activities in the host galaxy.

However, the luminosity of these galaxies is questionable, because of their potential gravitational magnification. Many apparent HyLIRGs have been found to be the result of lensing by large-area millimeter/submillimeter surveys (e.g., Negrello et al. 2010; Vieira et al. 2010; Bussmann et al. 2013; Wardlow et al. 2013; Cañameras et al. 2018) and follow-up studies (e.g., Yang et al. 2017; Zhang et al. 2018). For instance, the Herschel Astrophysical Terahertz Large Area Survey (Eales et al. 2010) revealed $\sim$1000 strongly lensed sources (González-Nuevo et al. 2012). After correcting for the lensing effect, many sources turn out to be of lower IR luminosity, thus are no longer HyLIRGs. For instance, Timmons et al. (2016) found that the apparent HyLIRG HATLAS J132427 is an intrinsic ULIRG, after correcting for the magnification factor of 5. Another apparent HyLIRG, SDP.81, has a magnification factor of $\sim$18, reconstructed with Atacama Large Millimeter/submillimeter Array (ALMA) data, and is indeed a ULIRG with an SFR of $\sim$100$M_\odot\ yr^{-1}$ (Rybak et al. 2020).

The high apparent IR luminosity can also be an effect of a collection of IR-bright sources. Luminous infrared galaxies (LIRGs; $L_{IR} > 10^{11} L_{\odot}$) have been extensively observed in the merging process (e.g., Chapman et al. 2003; Tacconi et al. 2006; Bothwell et al. 2010; Engel et al. 2010; Ivison et al. 2011, 2013; Riechers et al. 2011), which is also predicted by simulations (e.g., Swinbank et al. 2008; Narayanan et al. 2010; Hayward et al. 2011, 2012; McAlpine et al. 2019). State-of-the-art telescopes with subarcsecond-resolution powers, such as ALMA and the Very Large Array, have resolved some apparent HyLIRGs into multiple sources, confirming the resolved sources to be LIRGs or ULIRGs instead. For example, Fu et al. (2013) resolved two merging ULIRGs in the apparent HyLIRG 1HERMES S250 J022016.5-060143, which used to be considered as an unusually bright HyLIRG in the Herschel Multi-tiered Extragalactic Survey (HerMES; Oliver et al. 2012).

CO observations are crucial to studying the physical properties of these galaxies. First, they trace the immediate star-forming material in the host galaxy. This is connected to the feedback of AGNs, as controversial results have been reported on whether they drive out gas or accelerate the star formation efficiency (SFE; e.g., Kirkpatrick et al. 2019; Bischetti et al. 2021). Besides, they can reveal the direct feedback from quasars in the form of galactic-scale outflows, which are exhibited as broad line wings exceeding a velocity of 500 km s^{-1} (e.g., Feruglio et al. 2010; Cicone et al. 2012). Finally, Harris et al. (2012) have found that strongly lensed galaxies can be distinguished by CO line emission. Thus, we are able to estimate the lensing property of galaxies under limited resolution.

In this work, we conduct NOrthern Extended Millimeter Array (NOEMA) observations of the mid-J CO rotational emission ($J = 4 - 3$ or $J = 5 - 4$) and 2 mm dust continuum in six starburst apparent HyLIRG quasars at $z \sim 2.5$. The sample is selected from the quasar catalog of the Sloan Digital Sky Survey (SDSS) in the Stripe 82 field, with apparent HyLIRG-level IR luminosity from Herschel observations (Dong & Wu 2016). We use the millimeter observations to probe the molecular gas and dust properties in these sources and to identify if they are intrinsic or lensed starburst HyLIRG quasars.

The paper is organized as follows. In Section 2, we describe the sample selection, the observations, and the data reduction process. In Section 3, the observational results are presented, including the continuum and CO emission morphology and properties, and the optical-to-millimeter spectral energy distributions (SEDs) of our sample. In Section 4, we discuss the sample's location in the HyLIRG diagnostics, the spatial and velocity offsets of the sample between various tracers, and the estimated SFR and depletion time, followed by a summary in Section 5.

Throughout this paper, we adopt a ΛCDM cosmology, with $\Omega_m = 0.32$, $\Omega_{\Lambda} = 0.68$, $\Omega_k = 0$, and $H_0 = 67$ km s^{-1} Mpc^{-1} (Planck Collaboration et al. 2020). In addition, we adopt the Chabrier initial mass function (IMF; Chabrier 2003) for our SFR estimates.

2. Sample Selection and Observations

2.1. Sample Selection

We select six apparent starburst HyLIRG quasars from the catalog in Dong & Wu (2016). This sample was selected in the Stripe 82 field from the SDSS quasar catalogs (Schneider et al. 2010; Shen et al. 2011; Pâris et al. 2014), which were preselected to be brighter than $M_i = -22.0$ and have at least one optical line with FWHM larger than 1000 km s^{-1} (Type 1). These quasars were then crossmatched with the Herschel Stripe 82 Survey (HerS; Viero et al. 2014) by Dong & Wu (2016), and 207 showed Herschel SPIRE detections at 250, 350, and 500 μm. These wavelengths cover the spectral regions close to the peak of the cold dust emission at $z \sim 2.5$ and thus can better constrain the cold dust properties in the SED fitting. The AGN-subtracted IR luminosity $L_{IR, 8-1000 \mu m}$ was then calculated based on a graybody dust component (Dong & Wu 2016).

We then selected sources with $L_{IR, 8-1000 \mu m} > 10^{13} L_{\odot}$ (Table 1), i.e., apparent starburst HyLIRGs. To avoid possible gravitational lensing and blending issues, we further required the targets to be point sources in the SDSS images, without any close companion within 5″, which is slightly larger than the NOEMA resolution ($\sim$4″; D configuration). This way, we selected six starburst HyLIRG quasars from the Dong & Wu (2016) catalog, namely DW001 to DW006. All of the selected sources have spectroscopic redshifts between 2 and 3, corresponding to the peaks of cosmic evolution for both SF and AGN accretion (Förster Schreiber & Wuyts 2020). Some of them have multi-epoch observations by SDSS, including those from the Baryon Oscillation Spectroscopic Survey (BOSS; Eisenstein et al. 2011) and the Extended Baryon Oscillation Spectroscopic Survey (Dawson et al. 2016). For the convenience of later comparisons with millimeter observations, we use optical properties derived from the spectra taken at the closest time to our NOEMA observations.

The physical properties of the six quasars are listed in Table 1. The virial black hole mass listed in Table 1 was based on the broad C IV lines (Shen et al. 2011), with a typical $M_{BH} \gtrsim 10^9 M_{\odot}$ (except DW004), placing them among the most massive quasars. The bolometric luminosities (L_{bol}) of the selected sources are $10^{46.4-47.4}$ erg s^{-1}. Figure 1 shows their positions in the redshift–L_{bol} plane. Our sources have comparable bolometric luminosities with AGNs at similar redshifts from the literature.

2.2. Observations and Data Reduction

We observed our targets with NOEMA (S20BT; PI: Dai) in the 2 mm band with 10 antennas on 2020 June 6, 15, 19, and September 17 (Table 2). The compact D configuration was chosen to achieve the highest sensitivity.

We used the Herschel coordinates of the sources as the phase centers (Figure 2). The targets were observed with the PolyFix correlator with two sidebands of 7.744 GHz bandwidths. At $z =$ 2–3, the equivalent velocity coverage is $\sim$14,000–16,000 km s^{-1} in each sideband. We adjust the $\sim$140–160 GHz spectral windows (Table 2) to cover the ^{12}CO(4–3) (rest frequency 461.040 GHz) for $z < 2.5$ targets and ^{12}CO(5–4) (rest frequency 576.267 GHz) for $z > 2.5$ targets. The expected CO lines are set close to the center of one 3.8 GHz baseband. The native channel width was 2 MHz, and resampled to $\sim$20 MHz during the data calibration process, corresponding to $\sim$40 km s^{-1}.

We took advantage of the track-sharing mode and grouped our sources into two frequency tuning sets (DW001, DW002, DW003, and DW006 in S20BT001 and DW004 and DW005 in S20BT002). The observations on June 15 of S20BT001 were not used due to bad data quality. For S20BT001 and S20BT002, the phase and amplitude calibrators were

---

[11] μSFR ($M_{\odot}$ yr^{-1}) = 1.2×10^{-10} $\mu L_{IR,SB}$ ($L_{\odot}$), where $\mu L_{IR,SB}$ is the AGN-removed, pure starburst IR luminosity (converted from Kennicutt 1998), after applying a correction factor of 0.7 for the Chabrier IMF (Davé 2008).

Table 1
Source Properties

Source Name	Herschel Name[b]	SDSS Coordinates[a]		Herschel Coordinates[b]		$S_{250\mu m}$[b] (mJy)	$S_{350\mu m}$[b] (mJy)	$S_{500\mu m}$[b] (mJy)	$\log \mu L_{IR}$[c] ($L_\odot$)	$\log M_{BH}$[d] ($M_\odot$)	Redshift[e]
		α_{2000}	δ_{2000}	α_{2000}	δ_{2000}						
DW001	J0111.09-0038.8	01:11:05.56	−00:38:56.35	01:11:05.58	−00:38:54.50	40.6 ± 11.2	44.3 ± 10.9	48.0 ± 11.9	13.0 ± 0.14	9.7 ± 0.09	2.8617 ± 0.0003
DW002	J0134.04 + 0039.6	01:34:02.83	00:39:44.16	01:34:02.92	00:39:41.60	54.2 ± 11.4	83.1 ± 11.4	65.1 ± 12.4	13.1 ± 0.09	9.2 ± 0.37	2.5687 ± 0.0003
DW003	J0148.15−0010.2	01:48:09.64	−00:10:17.85	01:48:09.46	−00:10:14.90	81.7 ± 10.9	73.5 ± 11.0	76.1 ± 12.1	13.0 ± 0.06	9.8 ± 0.02	2.1528 ± 0.0004
DW004	J0156.72 + 0036.8	01:56:43.81	00:36:48.70	01:56:43.62	00:36:47.30	35.6 ± 10.2	36.3 ± 10.3	52.1 ± 11.0	13.1 ± 0.14	8.5 ± 0.09	2.0144 ± 0.0008
DW005	J0206.76 + 0105.1	02:06:46.34	01:05:06.40	02:06:46.31	01:05:05.57	78.8 ± 11.6	82.5 ± 11.0	68.1 ± 12.3	13.0 ± 0.05	9.4 ± 0.02	2.2665 ± 0.0003
DW006	J0212.30 + 0044.9	02:12:18.62	00:44:56.50	02:12:18.50	00:44:55.58	68.1 ± 10.7	77.5 ± 10.2	68.7 ± 11.0	13.1 ± 0.06	9.7 ± 0.02	2.8664 ± 0.0009

Notes.

[a] For DW001–DW006, if multiple SDSS/BOSS spectra are available, the observations with the closest observation dates to the NOEMA observations are used (i.e., MJDs of 55481, 58107, 58098, 52933, 58079, and 56979, respectively).

[b] The Herschel coordinates and flux densities at 250 μm ($S_{250\ \mu m}$), 350 μm ($S_{350\ \mu m}$), and 500 μm ($S_{500\mu m}$) are taken from the HerS catalog (Viero et al. 2014).

[c] Integrated between 8 and 1000 μm, derived from the SED fitting by Dong & Wu (2016), considering only the starburst graybody (i.e., cold dust) component. Note that we have derived improved values for these luminosities, $\mu L_{IR,SB}$, in Table 7.

[d] The virial black hole masses estimated from broad C IV lines (Shen et al. 2011; Dong & Wu 2016).

[e] SDSS spectroscopic redshifts, which are dominated by broad C IV lines (see Shen et al. 2011; Lyke et al. 2020; and the discussion in Section 4.3).
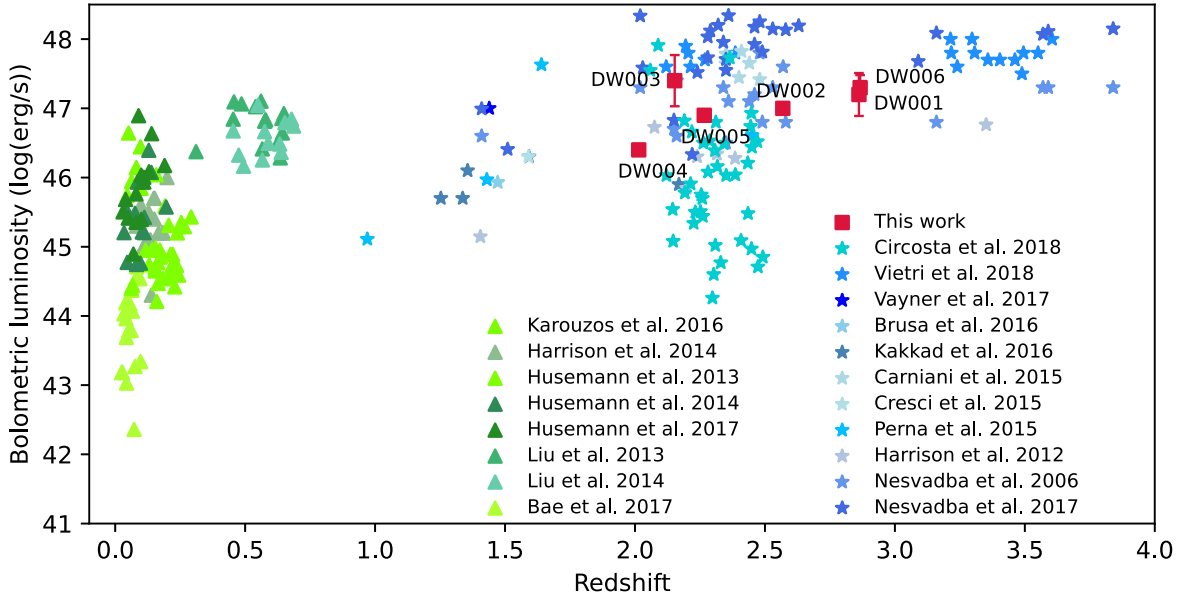
Figure 1. Redshifts of selected sources vs. their bolometric luminosities. The red filled squares are the six HyLIRG quasars with bolometric luminosities from Dong & Wu (2016). The triangles represent AGN systems at $z < 1$ (Husemann et al. 2013, 2014, 2017; Liu et al. 2013, 2014; Harrison et al. 2014; Karouzos et al. 2016; Bae et al. 2017). The filled stars represent high-redshift AGNs (Nesvadba et al. 2006, 2017; Alexander et al. 2010; Harrison et al. 2012; Carniani et al. 2015; Cresci et al. 2015; Perna et al. 2015; Brusa et al. 2016; Kakkad et al. 2016; Vayner et al. 2017; Vietri et al. 2018). The six sources we selected have comparable bolometric luminosities compared to known sources at similar redshifts.

Table 2
Observations

Tuning Set	Target Name	Observation Date	Exposure Time per Source (hr)	Rest Frequency[a] (GHz)	Baseline (m)	PWV[b] (mm)
S20BT001	DW001, DW002, DW003, DW006	2020 Jun 06	0.3	148.256	24–176	6–8
		2020 Jun 19	0.5			2–3
S20BT002	DW004, DW005	2020 Jun 17	0.8	141.500	24–176	5–9

Notes.
[a] Defined as the zero velocity in the lower sideband. For DW001, DW002, DW003, and DW006, the frequency coverage is 135.692–143.436 GHz (the lower sideband) and 151.180–158.924 GHz (the upper sideband). For DW004 and DW005, the frequency coverage is 144.576–152.320 GHz (the lower sideband) and 160.064–167.808 GHz (the upper sideband).
[b] Precipitable water vapor.

J0122-003 and 0215 + 015, respectively; the radio frequency calibrators were 3C454.3 and 3C84, respectively; and the flux calibrators were 1749 + 096, MWC349, 2010 + 723, 0106 + 013, and 0215 + 015.

We used the GILDAS CLIC and MAPPING packages to manually calibrate and reduce the data. The dust continuum was extracted from the uv tables and the flux was derived with a 2D Gaussian fit in the uv plane. A 5σ upper limit was assigned for nondetections, where σ is the 1σ dispersion of the brightness distribution within a $30'' \times 30''$ field centered at the source. The CO fluxes were extracted with 2D Gaussian fits on the uv plane for each channel, generated from the continuum-subtracted uv tables. The CO spectra were then constructed by combining the extracted fluxes of every channel. DW003 and DW005 show two CO-emitting components exceeding 4σ on the velocity-collapsed images, so we used two Gaussian components to extract the fluxes individually on the uv plane. On the extracted spectra, we fit Gaussian profiles ($\pm 1000\,\mathrm{km\,s^{-1}}$ around the channel of the peak flux) and derived the line properties, such as the FWHM, the peak flux density, and the integrated flux.

To test if the sources are resolved, we also extracted the continuum fluxes with a point-source model for comparison.

For DW001 and DW005, the point-source extracted fluxes are consistent with the 2D Gaussian extracted fluxes (within 1σ) and the FWHMs of the Gaussian profiles are smaller than the beam size. Therefore, we treat DW001 and DW005 as unresolved and use the point-source extracted fluxes. For DW002, DW003b, and DW006, the 2D Gaussian model gives a larger flux and cleaner residual. The typical fitted FWHM is $\sim 4''$, which is marginally resolved with our beam sizes of $\sim 3''-4''$, thus the fluxes measured with the Gaussian profile were used.

Figure 2 displays the dust continuum emission together with the CO emission images that were obtained by collapsing the data cubes within the fitted velocity ranges of the CO emission lines. We adopted natural weighting for the mapping process, set the cleaning threshold to be 50% of the 1σ noise of the $30'' \times 30''$ dirty map, and tried various degrees of tapering to all sources. For the CO emission of DW003, tapering creates larger synthesized beams ($6''.2 \times 3''.7$), thus concentrating the smeared-out flux and providing a higher peak-flux signal-to-noise ratio (S/N), which just exceeds our detection criterion of 5σ (from S/N ~ 4 to ~ 6). For other sources where the detection is not affected by tapering, we kept the original resolution (the typical beam size is $3''.5 \times 2''.5$; see Table 4).
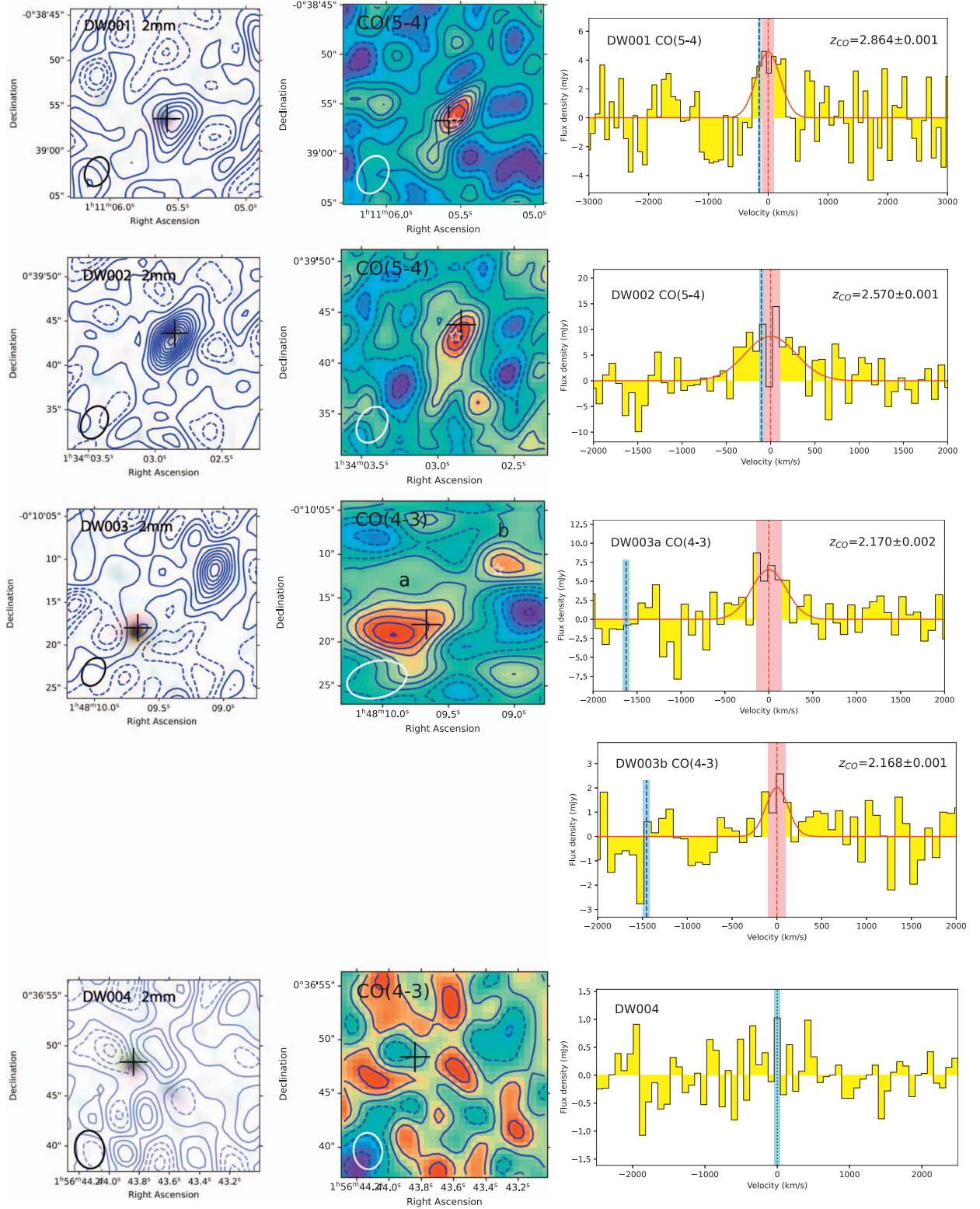
Figure 2. The 2 mm continuum (left) and CO (middle) maps and CO spectra (right) of DW001 to DW006 (from the top). In both maps, the solid contours represent positive values from 0, while the dashed contours are negative values from -1σ, with a 1σ spacing (see Table 3 for the σ values). The beam sizes are plotted in the bottom left corners. The quasars' SDSS positions are marked with black crosses, and the white stars in the CO maps mark the peak positions of the continuum. Note that for DW003, the peak of the dust continuum (DW003b) is significantly offset from the quasar's position (DW003a), while the CO emission comes mostly from the optical quasar (DW003a), though with a $4\rlap{.}''3$ offset. The right column shows the continuum-subtracted CO spectra, with a velocity resolution of $\sim$80 km s^{-1}. The red curves are the Gaussian fits for the lines. The vertical red dotted lines mark the fitted CO line centers, with their 1σ errors shown in pink shadows (Table 3). The vertical blue dotted lines and shades mark the expected CO frequency and 1σ dispersion based on the optical quasars' redshifts. For DW005a, the purple lines mark the positions for the two peaks, and the red vertical line represents the flux-weighted central position (see Table 3).
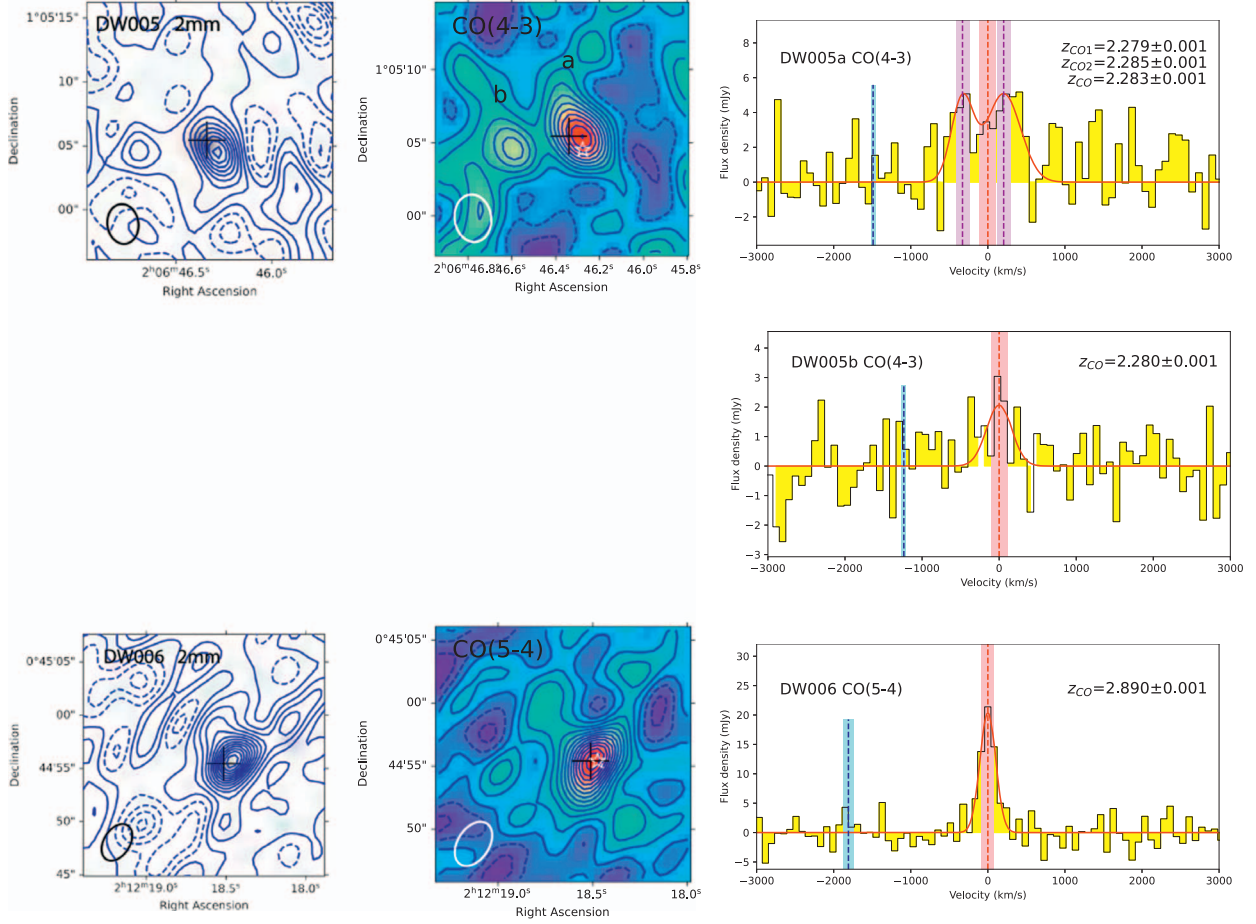
Figure 2. (Continued.)

Table 3
Observed CO and Dust Properties

Source Name	Targeted Line	Frequency Center[a] (GHz)	Line Width (km s^{-1})	Line Flux (Jy km s^{-1})	Peak Flux Density[b] (mJy)	Peak Flux (Jy beam km s^{-1})	CO Redshift	Continuum Flux Density[d] (mJy)
DW001	CO(5–4)	149.151	480 ± 160	2.3 ± 0.6	4.6 ± 1.1	1.5 ± 0.2	2.864 ± 0.001	0.28 ± 0.05
DW002	CO(5–4)	161.422	680 ± 170	6.2 ± 1.4	8.7 ± 1.9	1.8 ± 0.3	2.570 ± 0.001	0.96 ± 0.11
DW003a	CO(4–3)	145.441	430 ± 110	3.1 ± 0.7	6.8 ± 1.5	1.7 ± 0.3	2.170 ± 0.001	<0.24
DW003b		145.522	270 ± 100	0.6 ± 0.2	2.1 ± 0.7	1.1 ± 0.3	2.168 ± 0.001	0.54 ± 0.11
DW004	CO(4–3)	⋯	⋯	<1.3[c]	⋯	⋯	⋯	<0.29[c]
DW005a	CO(4–3)	140.441	530 ± 120	4.6 ± 0.8	5.1 ± 0.9	2.3 ± 0.3	2.283 ± 0.001	0.48 ± 0.06
DW005b		140.592	600 ± 230	1.2 ± 0.4	1.8 ± 0.6	1.2 ± 0.3	2.279 ± 0.001	<0.32[c]
DW006	CO(5–4)	148.146	250 ± 30	5.4 ± 0.6	20.3 ± 1.9	2.9 ± 0.2	2.890 ± 0.001	1.27 ± 0.12

Notes.
[a] With a typical error of ∼0.04–0.06 GHz. For those that have a fitted uncertainty of CO line frequency lower than 0.04 GHz, we use a spectral resolution of 0.04 GHz (corresponding to a velocity resolution of ∼80 km s^{-1}) as their error.
[b] Corresponding to a spectral resolution of ∼80 km s^{-1}.
[c] Upper limits are derived by 5σ background noise times one beam size.
[d] See the text for the way the continuum flux density is derived.

3. Dust Continuum, Molecular Gas Properties, and Morphology

3.1. Dust Continuum

We detect the dust continuum (peak flux density >5σ) in four of the six sources: DW001, DW002, DW005, and DW006. We also detect a >5σ dust continuum ∼90 kpc away from the DW003 optical position. The left column of Figure 2

shows the continuum contours overlaid on the optical images from SDSS. The measured dust continuum flux densities are listed in Table 3.

We note that the dust continuum of DW003 at the optical position (i.e., DW003a) is only 3.5σ. However, ∼10″ northeast, there is a >6σ continuum component (DW003b) without an optical counterpart, suggesting an optically obscured submillimeter galaxy (SMG). Given the tentative CO detection at the

Source Name	Beam		Separation			δv
	Size (arcsec × arcsec)	PA (deg)	$s_{\rm CO-mm}$ (arcsec)	$s_{\rm mm-opt}$ (arcsec)	$d_{\rm mm-opt}$ (kpc)	(km s^{-1})
(1)	(2)	(3)	(4)	(5)	(6)	(7)
DW001	3.9 × 2.9	−26	0.2 ± 0.6 NE	0.4 ± 0.5 W	3 ± 4	110 ± 80
DW002	3.5 × 2.5	149	0.2 ± 0.6 SE	1.6 ± 0.5 S	13 ± 4	80 ± 130
DW003a	6.2 × 3.7	103	⋯	4.3 ± 0.5 SE	36 ± 4	1480 ± 120
DW003b			⋯	10.6 ± 1.0 NW	88 ± 8	1610 ± 90
DW004	3.5 × 2.7	−173	⋯	⋯	⋯	⋯
DW005a	3.5 × 2.7	8	1.0 ± 0.6 S	1.4 ± 0.5 SW	12 ± 4	1420 ± 130
DW005b			−	4.3 ± 0.5 SE	35 ± 4	1160 ± 90
DW006	4.1 × 2.6	−33	0.6 ± 0.6 W	0.4 ± 0.5 W	3 ± 4	1810 ± 80

Notes. Column (1): source name. Column (2): size of the clean beam. Column (3): positional angle (PA) of the clean beam. Column (4): angular distance between the CO emission peak and the 2 mm continuum peak. Column (5): angular distance between the 2 mm continuum peak and the optical quasar position. Column (6): physical projected distance between the 2 mm continuum peak and the optical quasar position. Column (7): velocity difference between the CO emission line and optical redshifts, with both optical and CO redshift uncertainties considered (positive values indicate a redshifted CO emission compared to the optical lines). Since DW003a and DW005b do not have S/N >5 continuum detection, we only list the separation between the CO peak and the optical positions in columns (5) and (6). For DW003b, the spatial uncertainty is a combination of NOEMA pointing uncertainty and positional uncertainty. For the others, a 0″.5 spatial uncertainty is the pixel scale. For DW005a, the velocity offset is the average between the two peak positions, weighted by their relative fitted fluxes.

same redshift, DW003b is likely associated with the targeted quasar (Section 3.2). We note that the 250 μm HerS position is between DW003a and DW003b, indicating blending in the FIR dust emission. For DW004, we detect nothing at the 3σ level. For DW005, although the continuum is detected at 7σ, ~4″.7 east of the quasar, we find a companion with significant CO emission only (DW005b; see Section 3.2 and Figure 2). To calculate the continuum flux upper limits of DW004 and DW005b, we use the 5σ upper limit (see Section 2.2) times the synthesized beam size. The slightly extended 3σ continuum contour of DW006 could be a possible lensing effect, which will be discussed in Section 4.1. We also find spatial offsets and velocity shifts between the optical and millimeter observations, which will be described and discussed in Sections 3.3 and 4.3.

3.2. Molecular CO Emission

The central column of Figure 2 shows the molecular CO emissions, and the right column is the continuum-subtracted, integrated spectra. The CO(4–3) or CO(5–4) emissions are detected with a peak S/N level of ~6–13 for five of the six sources, except DW004. The measured line properties are listed in Table 3.

For DW001 and DW002, the CO(5–4) emissions both show a slightly extended structure along the major axis of the clean beam. Both have a CO emission that aligns well with the 2 mm dust continuum.

For DW003, there was no >5σ detection within the original beam resolution (4″.02 × 2″.78), so tapering was adopted. After tapering, a larger beam size (6″.16 × 3″.73) yields a 6σ CO(4–3) detection (DW003a), which extends to the southeast of the optical quasar position (the cross in Figure 2). This corresponds to a molecular gas reservoir up to 10″ (an S/N >3 region of ~80 kpc). To the northwest of DW003a, at the location of DW003b, we also detect a weak CO(4–3) emission of ~3σ. The ratio between the continuum flux density and CO peak flux density of DW003b (~0.3) is higher than other sources (<0.1; Table 3), which may indicate the existence of an obscured AGN. DW003a and DW003b have almost identical

emission-line frequencies, suggesting that they are in a pair system. The projected distance is ~110 kpc (~14″). Similar separations have been reported before (e.g., between NGC7679 and NGC7682 by Ricci et al. 2021), suggesting possible interaction between the two systems, which might have result in the extended CO morphology of DW003a.

DW004 is not detected in CO, despite integrating through a range of 2000 km s^{-1} around the expected frequency. The spectrum of DW004 is subtracted using a polygonal aperture covering the phase center, which is of similar size to the other detected sources (~10 beams). We estimate the upper limit of the CO(4–3) emission flux as 5σ noise times one beam size.

DW005 has two components. The higher-S/N CO(4–3) feature aligns well with the peak of the 2 mm dust continuum (DW005a). The related CO emission shows a double-peak line profile, with separation of ~650 km s^{-1}. The double-peaked profile may indicate either disk-like rotation in the system or two distinct velocity components. In the following analysis, we fit the two lines separately and also calculate an average velocity for DW005a, weighted by the fitted fluxes of the two lines. The average velocity corresponds to a redshift of 2.283 ± 0.001. We also find a potential second CO emitter (DW005b) ~5″ east of DW005a (Figure 2). DW005b has an integrated CO flux of >3σ, at an almost identical redshift of the bluer peak of DW005a, though not associated with any >3σ dust continuum (Section 3.1). The different line profiles of the two components suggest that they are not likely caused by gravitational lensing.

In DW006, the CO(5–4) line is detected at a ~10σ level with a relatively narrow width (FWHM = 250 km s^{-1}). Coincident dust continuum and optical positions, the strong emission, and the narrow FWHM are indicative of a lensed system, as will be discussed in Section 4.1.

3.3. Positional and Velocity Offsets

We find common (three out of five detected) positional offsets and velocity shifts between the NOEMA continuum emission and SDSS optical observations in our sample, as listed in Table 4. However, the moment maps, generated using

Table 5
Molecular Gas Properties

Source Name	$L'_{CO(4-3)}$ $(10^{10}\,\text{K km s}^{-1}\,\text{pc}^2)$	$L'_{CO(5-4)}$ $(10^{10}\,\text{K km s}^{-1}\,\text{pc}^2)$	$L'_{CO(1-0)}$ $(10^{10}\,\text{K km s}^{-1}\,\text{pc}^2)$	M_{H_2} $(10^{10}\,M_\odot)$
DW001	⋯	3.5 ± 1.0	5.1 ± 1.5	4.1 ± 1.2
DW002	⋯	8.0 ± 1.9	11.6 ± 2.7	9.2 ± 2.1
DW003a	4.6 ± 1.1	⋯	5.3 ± 1.3	4.2 ± 1.0
DW003b	0.8 ± 0.3	⋯	1.0 ± 0.4	0.8 ± 0.3
DW004	<1.0	⋯	<1.2	<1.0
DW005a	7.4 ± 1.3	⋯	8.5 ± 1.5	6.8 ± 1.2
DW005b	1.8 ± 0.6	⋯	2.1 ± 0.7	1.7 ± 0.6
DW006	⋯	8.3 ± 1.0	12.1 ± 1.4	9.7 ± 1.2

Notes. The factor μ is the possible gravitational amplification factor. M_{H_2} is estimated from $L'_{CO(1-0)}$, assuming a conversion factor $\alpha = 0.8\,M_\odot\,(\text{K km s pc}^2)^{-1}$. The errors on M_{H_2} do not include the uncertainty on α and the uncertainty on the conversion to the ground transition.

the GILDAS MAPPING package, do not show any significant signs of velocity components.

For DW001, DW002, DW005, and DW006, the peak positions of the 2 mm continuum are offset from the quasar optical positions by $\sim0\rlap{.}''4$–$1\rlap{.}''6$. We calculate the spatial uncertainties using

$$\delta\theta = \left(\frac{4}{\pi}\right)^{1/4} \frac{\theta_{\text{Beam}}}{\sqrt{8\ln 2} \times \text{S/N}_{\text{peak}}}, \qquad (1)$$

where $\delta\theta$ is the positional uncertainty, θ_{Beam} is the cleaned beam size ($3''$–$4''$), and S/N_{peak} is the S/N of the peak detection on the map (Reid et al. 1988). All our sources have consistent Gaia (Gaia Collaboration et al. 2016, 2021) positions with the SDSS coordinates, except for DW003 and DW005, whose Gaia positions are 40 mas north. Since 40 mas is negligible compared to the 2 mm uncertainties, in the following analysis and Table 4, all offsets are calculated based on the SDSS optical positions. The positional uncertainty $\delta\theta$, the NOEMA pointing accuracy of $0\rlap{.}''2$, the NOEMA pixel size of $0\rlap{.}''5$, and the SDSS positional uncertainty of $<0\rlap{.}''1$ together yield a spatial uncertainty of $1\rlap{.}''0$ for DW003b and $0\rlap{.}''5$ for the other sources. Since DW003a and DW005b have no significant dust continuum detection, in Table 4 (columns 5 and 6) we present their CO flux peak position offsets relative to the optical positions.

Column (2) in Table 4 lists the offsets of the peaks between the CO and dust continuum emissions ($s_{\text{CO-mm}}$) with an error calculated from the CO and continuum spatial detection uncertainties, NOEMA pointing accuracy, and pixel size. For DW001 and DW002, their offsets are consistent within the astrometric accuracy of NOEMA ($0\rlap{.}''2$). DW005a has a $1\rlap{.}''0$ positional offset, but of different direction compared to DW005b (south versus southeast), thus likely not due to the latter. Misaligned gas and dust components suggest that DW005a itself may be in a pair system, while DW005b is a third component outside the pair. Difference in the spatial distribution of the molecular gas and dust continuum has been observed with small separations at higher redshifts ($\leqslant1''$; e.g., Gururajan et al. 2022; Fogasy et al. 2022; Lamperti et al. 2022), though oftentimes larger offsets are observed between the optical and submillimeter components for both AGNs/quasars and star-forming galaxies (see Section 4.3).

In general, we find spatial offsets of $\sim1''$–$4''$ between the Herschel and the optical quasar positions. We note that the positional errors are at the $6''$ level, which propagate from the

pointing accuracy ($2''$; Pilbratt et al. 2010), spatial detection uncertainty ($\sim2''$), and the pixel size ($6''$ at 250 μm; Viero et al. 2014). Given the large positional errors, the optical–FIR offsets are not discussed later.

At $z \sim 2$–3, $1''$ corresponds to ~8 kpc. Thus, for our targets, the observed projected distance corresponds to 3–13 kpc. This offset is significant compared to the typical galaxy sizes at the cosmic noon (a few kiloparsecs; Förster Schreiber & Wuyts 2020). For targets with a companion 2 mm continuum component (DW003 and DW005), their offsets to the quasar positions range from 35 to 90 kpc, suggesting that the second millimeter source is likely another galaxy.

Velocity shifts are also observed between the optical and millimeter spectroscopic redshifts (Table 4). The red dashed lines in Figure 2 (right) mark the expected frequencies and ranges based on the SDSS spectroscopic redshifts and associated uncertainties. The differences between the optical and CO redshifts (i.e., δv) are all positive, corresponding to redshifted CO lines relative to the optical lines. In DW001 and DW002, the velocity difference is relatively small, with a large uncertainty, and can be treated as consistent, despite the relatively large spatial offset in DW002 (Columns (5) and (6) in Table 4). The velocity difference is large (1100–1800 km s^{-1}) for DW003, DW005, and DW006. We find significant velocity shifts, as compared to the redshift uncertainties, in DW003a and DW005a. These two systems may undergo volatile kinematic activities, possibly related to the secondary components. The origin and nature of these offsets will be further discussed in Section 4.3.

3.4. Molecular Gas Reservoir

We use the equation from Solomon et al. (1997) to calculate the CO(1–0) luminosity from the measured CO flux. To convert the observed mid-J CO luminosity to the CO(1–0) luminosity, $L'_{CO(1-0)}$, we adopt the conversion factors for quasars from Carilli & Walter (2013), i.e., $r_{41} = L'_{CO(4-3)}/L'_{CO(1-0)} = 0.87$ and $r_{51} = L'_{CO(5-4)}/L'_{CO(1-0)} = 0.69$.

To estimate the molecular gas mass, we adopt a linear relation between the L_{CO}' and H$_2$ masses (i.e., $M_{H_2} = \alpha L'_{CO(1-0)}$), assuming $\alpha = 0.8\,M_\odot\,(\text{K km s pc}^2)^{-1}$ (Dunne et al. 2022). For all detected targets (Table 5), this yields M_{H_2} of the order of $10^{10}\,M_\odot$. Note that these values are not corrected for possible magnification. The uncertainties listed in the table are based on the line measurement, without considering systematic uncertainties on the conversion factors. For instance, if we adopted $\alpha = 4.0\,M_\odot\,(\text{K km s pc}^2)^{-1}$, the

resulting M_{H_2} would have to be five times larger. In addition, we note that the conversion factors between different CO lines from Carilli & Walter (2013) are average values, with a large scatter (e.g., a scatter of 0.5 dex has been reported in CO(4–3) to CO(1–0); see, e.g., Bothwell et al. 2014; Banerji et al. 2018; Brusa et al. 2018).

3.5. SED Fitting

The SEDs for the six sources include fluxes and upper limits from SDSS (Alam et al. 2015; Ahumada et al. 2020), the UKIRT Infrared Deep Sky Survey (UKIDSS; Lawrence et al. 2007), the Wide Infrared Survey Explorer (WISE; Wright et al. 2010), and HerS (Viero et al. 2014; see Table 1). The measured 2 mm flux density greater than 5σ is used, otherwise a 5σ upper limit (Section 3.1) is adopted. We fit the SEDs of our HyLIRG quasars using the CIGALE code (Yang et al. 2022). We adopt an AGN component and a cold dust component in our SED fitting (Figure 3), with the CO redshifts as input. Table 6 lists the configuration for the fits.

We note that the FIR fluxes of DW003a in the HerS catalog may suffer from the blending of both DW003a and DW003b (see Section 3.1). However, the current Herschel resolution ($\sim$18″ at 250 μm; Viero et al. 2014) makes it difficult to assign the flux. Here, we assign 31% of the Herschel fluxes to DW003a, corresponding to DW003a and b's flux ratio in the 2 mm. At 500 μm, the beam size of SPIRE is $\sim$36″ (Viero et al. 2014). Considering possible contamination from nearby sources, we manually increase the error budget for 500 μm to 50% in the fit.

The properties derived from SED fitting are listed in Table 7. For DW001, DW002, and DW006, the $\mu L_{IR,SB}$ we calculate is consistent with the values in Dong & Wu (2016; Table 1) within $\sim$1σ. Their $\mu L_{IR,SB}$ still satisfy the HyLIRG definition. However, if a magnification factor of 5–10 is applied for DW006, as derived from Figure 4 in Section 4.1, its intrinsic $L_{IR,SB}$ will drop to the ULIRG level. For DW003a, in contrast to the $10^{13} L_\odot$ cold-dust IR luminosity reported by Dong & Wu (2016), the fitted $\mu L_{IR,SB}$ is also at the ULIRG level. In addition, the dust mass is of $10^8 M_\odot$, which is only $\sim$1% of the molecular gas mass (Table 5). This suggests a dusty companion source that contributes to the majority of the 2 mm emission. The $\mu L_{IR,SB}$ of DW004 is only $0.6 \times 10^{13} L_\odot$, about 50% lower than in Dong & Wu (2016). For all sources except DW003a, the fitted dust mass is of the order of $10^9 M_\odot$, indicating the dust-rich nature of these HyLIRG quasars.

We then estimate the μSFRs from $\mu L_{IR,SB}$ using the Kennicutt (1998) conversion after correcting for the Chabrier IMF. For all sources except DW003a and the undetected DW004, the calculated μSFR is $\sim$1700–2500$M_\odot$ yr^{-1} (Table 7), confirming the starburst nature of these HyLIRG quasars. We note that these $\mu L_{IR,SB}$ and μSFRs may be upper limits in some cases. Some quasars (e.g., $\sim$30%; Duras et al. 2017) are found to heat cold dust in the host galaxies and contribute more than 40% of the total IR luminosity (e.g., Schneider et al. 2015; Di Mascia et al. 2023).

4. Discussion

4.1. HyLIRG Diagnosis

Similar to the optical images, no signs of gravitational lensing, e.g., arcs or filaments, are detected in the millimeter dust continuum down to the resolution of 1″ of SDSS (Dawson et al. 2016). Therefore, we refer to the lensing diagnosis

diagram adapted from Harris et al. (2012), based on the relation between the apparent CO luminosities, $L'_{CO(1-0)}$, and the FWHM width, ΔV, of the CO emission lines. Figure 4 presents our sample, along with the CO data of 180 lensed and unlensed galaxies from the literature. When applicable, we recalculated the $L'_{CO(1-0)}$ using the same cosmology and conversion factors adopted in this study for consistency (see Section 3.4).

In Figure 4, galaxies clearly fall into two distinct populations: strongly lensed galaxies in the upper left and unlensed along the power-law relation. The unlensed or weakly lensed galaxies in general follow a virial relation:

$$L'_{CO(1-0)} = \frac{C(\Delta V/2.355)^2 R}{\alpha \cdot G}, \qquad (2)$$

where ΔV is the FWHM of the CO line in km s^{-1}, R is the radius of the CO emission region in parsecs, α is the conversion factor from $L'_{CO(1-0)}$ to solar mass in K km s^{-1}pc^2, G is the gravitational constant, and C is a constant related to the kinematics of the galaxy. We consider two extreme cases, using parameters suggested by Erb et al. (2006): $C = 2.1$, $R = 5$ kpc, and $\alpha = 4.6$ for a disk model; and $C = 5$, $R = 2$ kpc, and $\alpha = 1.0$ for a spherical model. Both models are plotted with dotted lines in Figure 4, which nicely bracket the majority of the unlensed and slightly lensed galaxies.

The solid line in Figure 4 represents the best-fit relation $L'_{CO} = 5.4 \times \Delta V^2$ derived by Bothwell et al. (2013) and also applied by, e.g., Zavala et al. (2015) and Neri et al. (2020). The dashed line represents the best-fit relation from Harris et al. (2012), i.e., $L'_{CO(1-0)}$ (K km s^{-1} pc^2) = $(\Delta V/400$ km s$^{-1})^{1.7} \times 10^{11}/3.5$. In our sample, four out of the five CO-detected sources are safely located in the unlensed or at most weakly lensed region. For DW005a, whose CO emission shows double peaks, the separation between the two peaks was used as its linewidth. Despite the large error bars, the two possible companions, DW003b and DW005b, also fall in the unlensed region.

For objects with multiple CO lines observed (e.g., Bothwell et al. 2013), we calculate the low-J (filled circle) and mid-J (triangle) emissions separately, and mark both on the diagram, using $L'_{CO}/L'_{CO(1-0)}$ ratios from Carilli & Walter (2013) for quasars and SMGs. Detections with S/N $\leqslant$ 3 (tentative detections) are not plotted.

Based on the L'_{CO}–ΔV diagram, DW001, DW002, DW003a, DW005a, and two possible companions (DW003b and DW005b) fall in the unlensed power-law region, thus they are likely unlensed or at most weakly lensed, intrinsic HyLIRGs. DW004 is undetected, thus not plotted. DW006 is likely strongly lensed, with an estimated magnification factor of $\sim$5–10, based on the offset from the power-law relation, making it a ULIRG system instead.

4.2. Depletion Time of the HyLIRGs

Based on the gas mass and SFR calculated in Sections 3.4 and 3.5, we estimate the gas depletion time:

$$\tau_{dep} = \frac{M_{H_2}}{SFR}. \qquad (3)$$

The calculated τ_{dep} (Table 7) ranges between 20 and 60 Myr, similar to other starburst galaxies (tens of Myr; e.g., Daddi et al. 2010; Combes et al. 2013), for all of our sources except DW003a. This τ_{dep} range is much shorter than the lifetime of a galaxy ($\sim$10 Gyr for elliptical galaxies; De Lucia et al. 2006).
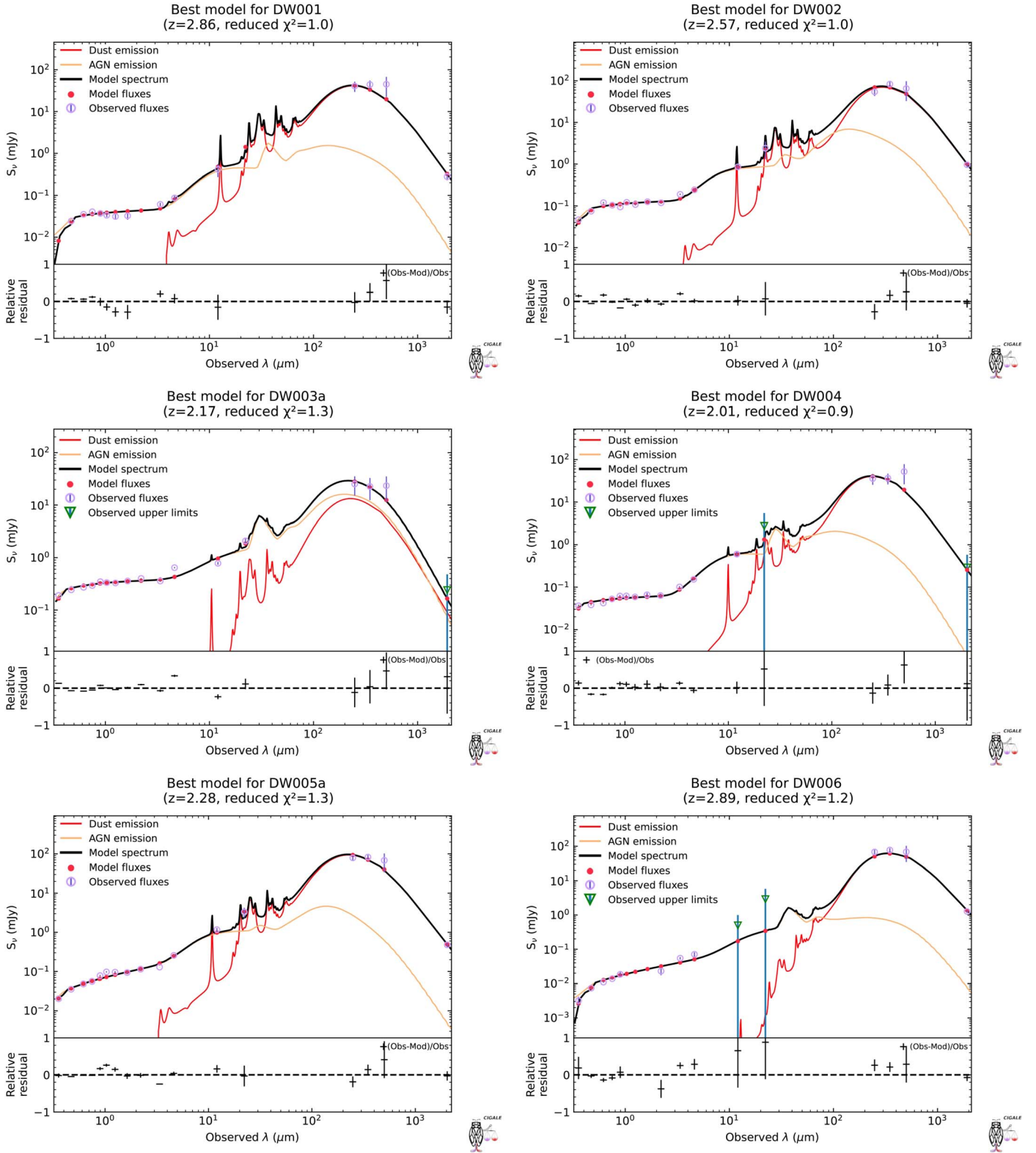
Figure 3. SEDs of our HyLIRG Quasar sample. The FIR dust emission is plotted in red, while the AGN component is in orange and in solid black is the composite SED. The violet empty circles mark the observed photometric data points, with upper limits shown in the downward triangles. Besides the NOEMA 2 mm continuum fluxes, the data points are from SDSS, UKIDSS, WISE, Herschel, and ALMA (see Section 3.5).

This is consistent with the scenario that HyLIRG quasars are in a short transitional phase in the early formation of the massive elliptical galaxies (Fu et al. 2013). We also note that if a Salpeter IMF is applied, the SFR would also increase by ∼0.15 dex

(Davé 2008), resulting in even shorter $\tau_{\rm dep}$ of ∼15–40 Myr. We also note that, as mentioned in Section 3.4, the depletion time could be up to 5 times longer if, instead of 0.8, a CO–H_2 conversion factor α of 4.0 $M_\odot$(K km s^{-1} pc^2)$^{-1}$ is adopted.
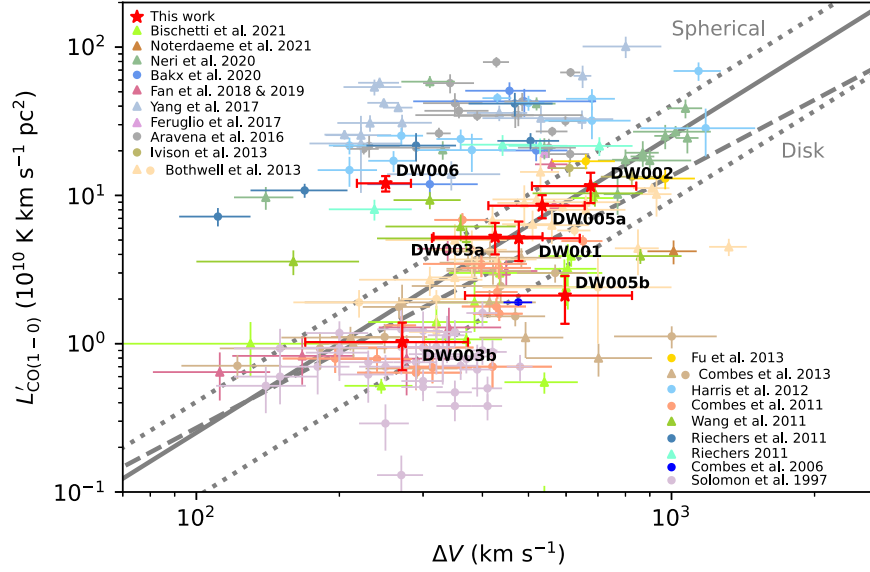
Figure 4. $L'_{CO(1-0)}$ vs. the CO FWHM (ΔV) for our sample of six HyLIRG quasars and 180 galaxies from the literature, including lensed and unlensed SMGs and DSFGs (Harris et al. 2012; Bothwell et al. 2013; Aravena et al. 2016; Yang et al. 2017; Bakx et al. 2020), local/low-to-mid-z ULIRGs (Solomon et al. 1997; Combes et al. 2006, 2011, 2013), and high-z quasars and companions (Wang et al. 2010; Riechers 2011; Riechers et al. 2011; Feruglio et al. 2017; Fan et al. 2018, 2019; Bischetti et al. 2021; Noterdaeme et al. 2021). Data points using CO high-J transitions ($J \geqslant 3$) are marked with triangles and converted to CO(1–0) using the same factors as in this paper (i.e., Carilli & Walter 2013), while data points using CO $J \leqslant 2$ transitions are marked with filled circles. The solid and dashed lines represent the approximate best-fitting quadratic relationships from Bothwell et al. (2013) and Harris et al. (2012), respectively. The dotted lines represent the virial relations assuming spherical and disk models.

Table 6
CIGALE Parameters for HyLIRG Quasar Candidates

Module	Parameter	Symbol	Values
Cold dust emission: Draine et al. (2014)	Mass fraction of Polycyclic Aromatic Hydrogen (PAH)	q_{PAH}	0.47, 1.77, 3.19, 5.95, 7.32
	Minimum radiation field	U_{min}	0.1, 5.0, 10, 15, 20, 30, 40, 50
	Power-law slope	α	1.0, 1.5, 2.0, 2.5, 3.0
	Luminated fraction	γ	0.10, 0.25, 0.50, 0.75, 0.99
AGN emission: Fritz et al. (2006)	AGN fraction	f_{AGN}	0.1, 0.2, 0.3, 0.4, 0.5, 0.6, 0.7, 0.8
	Optical depth	τ	0.1, 3.0, 10.0
	Beta	β	−1.0, −0.5, 0.0
	Gamma	γ	0.0, 2.0, 4.0, 6.0
	Angle between equatorial axis and line of sight (°)	ψ	60.10, 70.10, 80.10, 89.99
	Optical slope power-law index	δ	−1, −0.5, 0.0, 0.5, 1
	Emissivity index		1.6, 1.8, 2.0, 2.2
	Temperature of the polar dust (K)		80, 100, 120

Table 7
SED Fitting Results

Name	$f_{IR,AGN}$	$\mu L_{IR,SB}$ $(10^{13} L_\odot)$	μSFR $(M_\odot \, yr^{-1})$	τ_{dep} (Myr)	μM_{dust} $(10^8 M_\odot)$
DW001	0.16 ± 0.07	1.7 ± 0.8	2000 ± 1000	20 ± 10	9 ± 2
DW002	0.24 ± 0.06	1.9 ± 0.6	2200 ± 700	40 ± 20	35 ± 8
DW003a	0.70 ± 0.09	0.3 ± 0.1	400 ± 200	110 ± 50	7 ± 6
DW004	0.25 ± 0.07	0.6 ± 0.2	700 ± 300	<10	15 ± 10
DW005a	0.11 ± 0.03	2.1 ± 0.4	2500 ± 500	30 ± 10	21 ± 4
DW006	0.10 ± 0.01	1.4 ± 0.1	1700 ± 100	60 ± 10	48 ± 8

Notes. $f_{IR,AGN}$ is the fraction of AGN emission in the total IR luminosity estimated from SED fitting with the CIGALE code. $\mu L_{IR,SB}$ is the AGN-removed, starburst-dominant IR luminosity. μM_{dust} is the fitted galactic dust mass. The luminosities, SFRs, and masses are apparent quantities not corrected for possible gravitational lensing effects. τ_{dep} is the depletion time calculated from Equation (3).
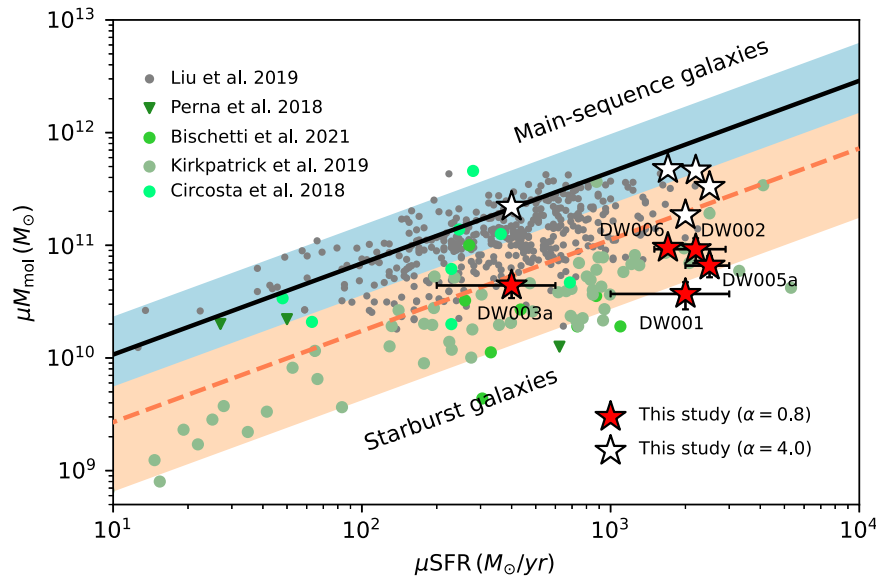
Figure 5. The inverse integrated Kennicutt–Schmidt relation. The blue strip represents the relation for main-sequence (MS) galaxies, with a dispersion of 0.3 dex. The solid black line is the MS relation consistent with Figure 3 in Tacconi et al. (2020) at $z \sim 2.5$. The dashed orange line represents the MS relation offset by 0.6 dex to represent the starburst galaxies. The pink strip marks the starburst regions, whose lower border represents the extreme starburst galaxies with an SFE $\sim$15 times higher than that of the MS galaxies (Sargent et al. 2014). Our five CO-detected quasars all fall in the starburst region, with a CO–H_2 conversion factor $\alpha = 0.8 M_\odot (\mathrm{K\ km\ s^{-1}\ pc^2})^{-1}$ (red stars), similar to other starburst galaxies (Tacconi et al. 2020). They will fall in a transitional region between starburst and MS galaxies if $\alpha = 4.0 M_\odot (\mathrm{K\ km\ s^{-1}\ pc^2})^{-1}$ is adopted (white stars). The gray dots are the star-forming galaxies in the COSMOS deep field from Liu et al. (2019) at $z = 2$–3 plotted for comparison. The filled circles and triangles (upper limits) are AGNs from the literature (Perna et al. 2018; Kirkpatrick et al. 2019; Bischetti et al. 2021; Circosta et al. 2021). No correction of gravitational magnification is applied to the sources.

In Figure 5, we compare the inverse integrated Kennicutt–Schmidt relation between the molecular gas mass and μSFR of our sources, and observations from the literature. Using μM_{H_2} as a proxy for the total molecular gas mass, we find that the SFEs of all CO-detected sources follow the trend for starburst galaxies, similar to AGNs from the literature.

4.3. Origin of the Observed Positional and Velocity Offsets

In Section 3.3, we present the spatial offset and velocity shifts between the optical quasars and the millimeter dust and molecular gas components. In this section, we investigate the possible causes of these shifts. Similar offsets have been ubiquitously observed in quasars and star-forming galaxies, where the locations of the molecular CO or dust components deviate from either the galaxies' optical positions or redshifts, or both (e.g., Krips et al. 2005; Clements et al. 2009; Combes et al. 2013; Iono et al. 2016; Chiaberge et al. 2017; Ikarashi et al. 2017; Magdis et al. 2017; Barthel et al. 2018; Vayner et al. 2021).

One likely explanation for the systematic redshifted CO velocity is the known blueshift in the broad C IV emission lines in the quasar system, whose peak is often blueshifted with respect to narrowline emissions, such as [O III], used as the representative systematic redshift of the quasar system when available (see, e.g., Richards et al. 2011; Coatman et al. 2017; Vietri et al. 2020), and to cold gas tracers such as [C III] and CO (see, e.g., Bischetti et al. 2017; Trakhtenbrot et al. 2017; Schindler et al. 2020; Circosta et al. 2021). For our sources at $z \sim 2$–3, indeed the redshift determination from SDSS is highly reliable on the broad C IV broad emission lines, partly due to the absence of [O III] or [Ne V] lines in the wavelength coverage. We double checked the spectra of DW002, DW003, and DW005, whose Mg II broad emission lines are also well detected. We find that all of the Mg II lines are $\lesssim 1000\ \mathrm{km\ s^{-1}}$

redshifted from the SDSS redshifts, fixed as the Gaussian center wavelength when fitting the Mg II line profiles. If we treat the Mg II redshift as the quasar's representative redshift, and remove any velocity difference from the CO optical velocity offsets, the offsets now become -700, 600, and 500 $\mathrm{km\ s^{-1}}$ for DW002, DW003a, and DW005, respectively. We note that the intrinsic blueshift of the broad-line region (BLR) could be as large as $\sim$2000 $\mathrm{km\ s^{-1}}$ (e.g., Vietri et al. 2018; Schindler et al. 2020), which could explain the velocity shifts observed in our quasar sample. A comparison of optical and CO redshifts on broad-line spectra is demonstrated in Figure 6.

Another scenario involves unresolved mergers in the HyLIRG quasar systems, as in the cases in Krips et al. (2005) and a number of similar targets (i.e., a powerful AGN with a CO-rich merging partner; e.g., Walter et al. 2004; De Breuck et al. 2005). Merging galaxies with a dust-free quasar and an optically obscured SMG could explain the observed offsets, both positionally and spectroscopically, with the SMGs contributing the majority of the observed CO and dust emissions. If two galaxies are in the later stage of a merger, they cannot be resolved under the current resolution ($\sim 3\rlap{.}''5 \times 2\rlap{.}''5$), even if the CO emission is centered at a second component slightly offset from the quasar location. The SMG + quasar scenario could also explain the observed velocity offsets up to several hundred kilometers per second. The merging of two gas-rich galaxies can trigger starburst and explain the observed HyLIRG-level luminosities, as has been demonstrated in the cases of ULIRGs (e.g., Riechers 2011; Ivison et al. 2019; Huang et al. 2023). In fact, DW003a has extended CO morphology, implying a second gas clump or galaxy at almost identical redshifts at a distance of $\sim$90 kpc from the main component. The double-peaked CO line profile of DW005a indicates disk-like rotation or two distinct velocity components. This offers indirect evidence to support the merger scenario.
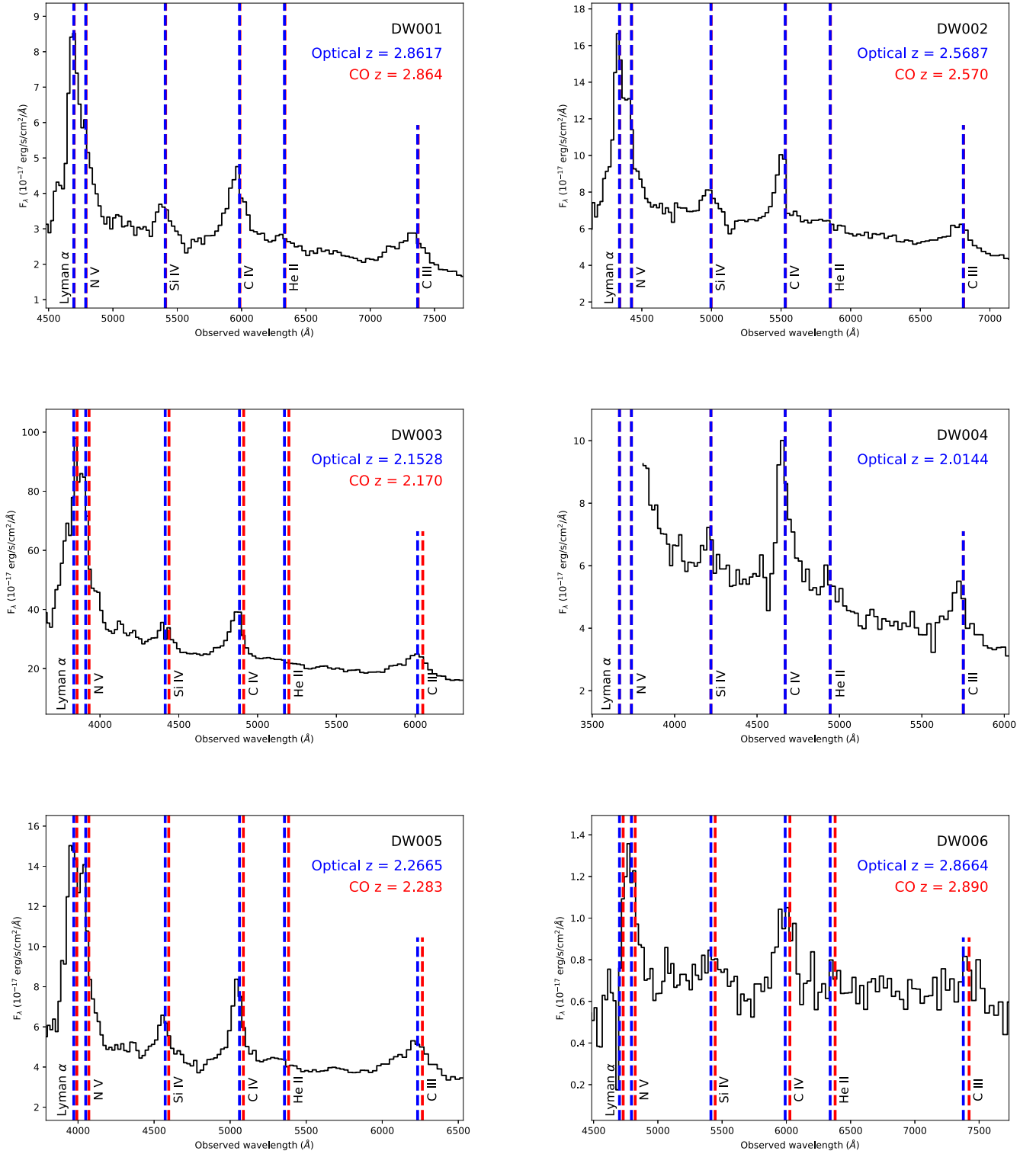
Figure 6. Broad-emission-line spectra of DW001–DW006. The red dashed vertical lines mark the CO redshifts, and the blue dashed vertical lines mark the optical redshifts from SDSS (Table 1). For DW001 and DW002, the optical and CO redshifts are consistent and overlaid with each other. For DW003, DW005, and DW006, the CO lines are redshifted from the peaks of optical lines.

Finally, we cannot rule out the recoiling black holes scenario: the central black hole being ejected with the BLR during galaxy merging, with the narrow lines still lagging behind in the center of the galaxy, as well as the molecular gas (Komossa 2012). Velocity offsets generated by this effect can be of the order of

$100–1000 \, \mathrm{km \, s^{-1}}$ (as discussed in Chiaberge et al. 2017), which is consistent with the observed velocity offset in our sample. However, simulation suggests the probability of such an event is low (only $<10\%$ of recoiling black holes formed from binary black holes have velocity $>1000 \, \mathrm{km \, s^{-1}}$; Civano et al. 2010).

Liu et al.

5. Conclusion

In this paper, we report NOEMA observations of a sample of six apparent HyLIRG quasars, selected as SDSS broad-emission-line quasars with Herschel IR emissions at the HyLIRG level. Five out of the six quasars are detected or marginally detected in CO(5–4) or CO(4–3), and four show well-detected dust continuum emissions.

The main conclusions of this paper are summarized as follows:

1. We confirm that out of the five CO-detected quasars, four are consistent with being unlensed HyLIRGs, based on their locations on the CO(1–0) luminosity ($L'_{CO(1-0)}$) versus linewidth (ΔV) diagram. One source, DW006, is located well above the relation, suggesting a gravitationally amplified galaxy with $\mu \sim 5$–10.

2. Based on the cold molecular gas observations, we derive the molecular gas mass of our HyLIRG quasars to be $M_{H_2} \sim 10^{10} M_\odot$, with a depletion timescale of $\sim$20–110 Myr, using a $M_{H_2}/L'_{CO(1-0)}$ conversion factor of 0.8 $M_\odot$(K km s pc^2)$^{-1}$. All of our CO-detected sources align well with starbursts.

3. The majority of our sources show significant positional (3–35 kpc) offsets between the optical (quasar) and millimeter (dust/CO) emission peaks. Most of them also have CO lines redshifted by 1000–2000 km s^{-1} in velocity compared to the optical redshifts, likely related to the blueshifted BLRs observed in quasars. The observed spatial offsets and velocity shifts are consistent with the scenario that some of our HyLIRG quasars are in a merger system with an optically obscured SMG and an optically bright quasar. The high SFR in these systems can be explained by the merger-triggered starburst.

Our HyLIRG quasar sample offers a special population for investigating the connection between quasars and SF activities in the most extreme starburst galaxies. Their high molecular mass and likely unlensed nature indicate that these targets are in a fast transitional phase in between starburst and normal star-forming galaxies, while the common positional offset and spectroscopic velocity shifts indicate possible merging systems or complicated kinematics. High-resolution observations, such as those from JWST and ALMA, will be helpful to identify more intrinsic HyLIRG quasar systems and to reveal their true nature.

ORCID iDs

Feng-Yuan Liu ● https://orcid.org/0000-0003-1386-3676
Y. Sophia Dai ● https://orcid.org/0000-0002-7928-416X
Alain Omont ● https://orcid.org/0000-0002-4721-3922
Daizhong Liu ● https://orcid.org/0000-0001-9773-7479
Pierre Cox ● https://orcid.org/0000-0003-2027-8221
Roberto Neri ● https://orcid.org/0000-0002-7176-4046
Chentao Yang ● https://orcid.org/0000-0002-8117-9991
Xue-Bing Wu ● https://orcid.org/0000-0002-7350-6913
Jia-Sheng Huang ● https://orcid.org/0000-0001-6511-8745

References

Ahumada, R., Prieto, C. A., Almeida, A., et al. 2020, ApJS, 249, 3
Alam, S., Albareti, F. D., Allende Prieto, C., et al. 2015, ApJS, 219, 12
Alexander, D. M., Swinbank, A. M., Smail, I., et al. 2010, MNRAS, 402, 2211
Aravena, M., Spilker, J. S., Bethermin, M., et al. 2016, MNRAS, 457, 4406
Bae, H.-J., Woo, J.-H., Karouzos, M., et al. 2017, ApJ, 837, 91
Bakx, T. J. L. C., Dannerbauer, H., Frayer, D., et al. 2020, MNRAS, 496, 2372
Banerji, M., Jones, G. C., Wagg, J., et al. 2018, MNRAS, 479, 1154
Banerji, M., McMahon, R. G., Hewett, P. C., et al. 2013, MNRAS, 429, L55
Barthel, P. D., Versteeg, M. J. F., Podigachoski, P., et al. 2018, ApJL, 866, L3
Bischetti, M., Feruglio, C., Piconcelli, E., et al. 2021, A&A, 645, A33
Bischetti, M., Piconcelli, E., Vietri, G., et al. 2017, A&A, 598, A122
Bothwell, M. S., Chapman, S. C., Tacconi, L., et al. 2010, MNRAS, 405, 219
Bothwell, M. S., Smail, I., Chapman, S. C., et al. 2013, MNRAS, 429, 3047
Bothwell, M. S., Wagg, J., Cicone, C., et al. 2014, MNRAS, 445, 2599
Brusa, M., Cresci, G., Daddi, E., et al. 2018, A&A, 612, A29
Brusa, M., Perna, M., Cresci, G., et al. 2016, A&A, 588, A58
Bussmann, R. S., Pérez-Fournon, I., Amber, S., et al. 2013, ApJ, 779, 25
Cañameras, R., Yang, C., Nesvadba, N. P. H., et al. 2018, A&A, 620, A61
Carilli, C. L., & Walter, F. 2013, ARA&A, 51, 105
Carniani, S., Marconi, A., Maiolino, R., et al. 2015, A&A, 580, A102
Casey, C. M., Berta, S., Béthermin, M., et al. 2012, ApJ, 761, 139
Chabrier, G. 2003, PASP, 115, 763
Chapman, S. C., Windhorst, R., Odewahn, S., et al. 2003, ApJ, 599, 92
Chiaberge, M., Ely, J. C., Meyer, E. T., et al. 2017, A&A, 600, A57
Cicone, C., Feruglio, C., Maiolino, R., et al. 2012, A&A, 543, A99
Circosta, C., Mainieri, V., Lamperti, I., et al. 2021, A&A, 646, A96
Civano, F., Elvis, M., Lanzuisi, G., et al. 2010, ApJ, 717, 209
Clements, D. L., Petitpas, G., Farrah, D., et al. 2009, ApJL, 698, L188
Coatman, L., Hewett, P. C., Banerji, M., et al. 2017, MNRAS, 465, 2120
Combes, F., García-Burillo, S., Braine, J., et al. 2006, A&A, 460, L49
Combes, F., García-Burillo, S., Braine, J., et al. 2011, A&A, 528, A124
Combes, F., García-Burillo, S., Braine, J., et al. 2013, A&A, 550, A41
Cresci, G., Mainieri, V., Brusa, M., et al. 2015, ApJ, 799, 82
Daddi, E., Elbaz, D., Walter, F., et al. 2010, ApJL, 714, L118
Dai, Y. S., Bergeron, J., Elvis, M., et al. 2012, ApJ, 753, 33
Dai, Y. S., Wilkes, B. J., Bergeron, J., et al. 2018, MNRAS, 478, 4238
Davé, R. 2008, MNRAS, 385, 147
Dawson, K. S., Kneib, J.-P., Percival, W. J., et al. 2016, AJ, 151, 44
De Breuck, C., Downes, D., Neri, R., et al. 2005, A&A, 430, L1
De Lucia, G., Springel, V., White, S. D. M., et al. 2006, MNRAS, 366, 499
Di Mascia, F., Carniani, S., Gallerani, S., et al. 2023, MNRAS, 518, 3667
Dong, X. Y., & Wu, X.-B. 2016, ApJ, 824, 70
Draine, B. T., Aniano, G., Krause, O., et al. 2014, ApJ, 780, 172
Dunne, L., Maddox, S. J., Papadopoulos, P. P., et al. 2022, MNRAS, 517, 962
Duras, F., Bongiorno, A., Piconcelli, E., et al. 2017, A&A, 604, A67
Eales, S., Dunne, L., Clements, D., et al. 2010, PASP, 122, 499
Eisenstein, D. J., Weinberg, D. H., Agol, E., et al. 2011, AJ, 142, 72
Engel, H., Tacconi, L. J., Davies, R. I., et al. 2010, ApJ, 724, 233
Erb, D. K., Steidel, C. C., Shapley, A. E., et al. 2006, ApJ, 646, 107
Fabian, A. C. 2012, ARA&A, 50, 455
Fan, L., Knudsen, K. K., Fogasy, J., et al. 2018, ApJL, 856, L5
Fan, L., Knudsen, K. K., Han, Y., et al. 2019, ApJ, 887, 74
Feruglio, C., Ferrara, A., Bischetti, M., et al. 2017, A&A, 608, A30
Feruglio, C., Maiolino, R., Piconcelli, E., et al. 2010, A&A, 518, L155
Fogasy, J., Knudsen, K. K., & Varenius, E. 2022, A&A, 660, A60
Förster Schreiber, N. M., & Wuyts, S. 2020, ARA&A, 58, 661
Fritz, J., Franceschini, A., & Hatziminaoglou, E. 2006, MNRAS, 366, 767
Fu, H., Cooray, A., Feruglio, C., et al. 2013, Natur, 498, 338
Gaia Collaboration, Brown, A. G. A., Vallenari, A., et al. 2016, A&A, 595, A2
Gaia Collaboration, Brown, A. G. A., Vallenari, A., et al. 2021, A&A, 649, A1
González-Nuevo, J., Lapi, A., Fleuren, S., et al. 2012, ApJ, 749, 65
Gururajan, G., Béthermin, M., Theulé, P., et al. 2022, A&A, 663, A22
Harris, A. I., Baker, A. J., Frayer, D. T., et al. 2012, ApJ, 752, 152

Harrison, C. M., Alexander, D. M., Mullaney, J. R., et al. 2014, MNRAS, 441, 3306
Harrison, C. M., Alexander, D. M., Swinbank, A. M., et al. 2012, MNRAS, 426, 1073
Hayward, C. C., Jonsson, P., Kereš, D., et al. 2012, MNRAS, 424, 951
Hayward, C. C., Kereš, D., Jonsson, P., et al. 2011, ApJ, 743, 159
Huang, J.-S., Li, Z-J., Cheng, C., et al. 2023, ApJ, 949, 83
Husemann, B., Davis, T. A., Jahnke, K., et al. 2017, MNRAS, 470, 1570
Husemann, B., Jahnke, K., Sánchez, S. F., et al. 2014, MNRAS, 443, 755
Husemann, B., Wisotzki, L., Sánchez, S. F., et al. 2013, A&A, 549, A43
Ikarashi, S., Caputi, K. I., Ohta, K., et al. 2017, ApJL, 849, L36
Iono, D., Yun, M. S., Aretxaga, I., et al. 2016, ApJL, 829, L10
Ivison, R. J., Page, M. J., Cirasuolo, M., et al. 2019, MNRAS, 489, 427
Ivison, R. J., Papadopoulos, P. P., Smail, I., et al. 2011, MNRAS, 412, 1913
Ivison, R. J., Swinbank, A. M., Smail, I., et al. 2013, ApJ, 772, 137
Kakkad, D., Mainieri, V., Padovani, P., et al. 2016, A&A, 592, A148
Karouzos, M., Woo, J.-H., & Bae, H.-J. 2016, ApJ, 819, 148
Kennicutt, R. C. 1998, ApJ, 498, 541
Kirkpatrick, A., Sharon, C., Keller, E., et al. 2019, ApJ, 879, 41
Komossa, S. 2012, AdAst, 2012, 364973
Kormendy, J., & Ho, L. C. 2013, ARA&A, 51, 511
Krips, M., Eckart, A., Neri, R., et al. 2005, A&A, 439, 75
Lamperti, I., Pereira-Santaella, M., Perna, M., et al. 2022, A&A, 668, A45
Laor, A., & Draine, B. T. 1993, ApJ, 402, 441
Lawrence, A., Warren, S. J., Almaini, O., et al. 2007, MNRAS, 379, 1599
Liu, D., Schinnerer, E., Groves, B., et al. 2019, ApJ, 887, 235
Liu, G., Zakamska, N. L., Greene, J. E., et al. 2013, MNRAS, 430, 2327
Liu, G., Zakamska, N. L., & Greene, J. E. 2014, MNRAS, 442, 1303
Lyke, B. W., Higley, A. N., McLane, J. N., et al. 2020, ApJS, 250, 8
Ma, Z., & Yan, H. 2015, ApJ, 811, 58
Magdis, G. E., Rigopoulou, D., Daddi, E., et al. 2017, A&A, 603, A93
McAlpine, S., Smail, I., Bower, R. G., et al. 2019, MNRAS, 488, 2440
Narayanan, D., Hayward, C. C., Cox, T. J., et al. 2010, MNRAS, 401, 1613
Negrello, M., Hopwood, R., De Zotti, G., et al. 2010, Sci, 330, 800
Neri, R., Cox, P., Omont, A., et al. 2020, A&A, 635, A7
Nesvadba, N. P. H., Drouart, G., De Breuck, C., et al. 2017, A&A, 600, A121
Nesvadba, N. P. H., Lehnert, M. D., Eisenhauer, F., et al. 2006, ApJ, 650, 693
Noterdaeme, P., Balashev, S., Combes, F., et al. 2021, A&A, 651, A17
Oliver, S. J., Bock, J., Altieri, B., et al. 2012, MNRAS, 424, 1614
Pâris, I., Petitjean, P., Aubourg, É., et al. 2014, A&A, 563, A54
Perna, M., Brusa, M., Salvato, M., et al. 2015, A&A, 583, A72

Perna, M., Sargent, M. T., Brusa, M., et al. 2018, A&A, 619, A90
Pilbratt, G. L., Riedinger, J. R., Passvogel, T., et al. 2010, A&A, 518, L1
Planck Collaboration, Aghanim, N., Akrami, Y., et al. 2020, A&A, 641, A6
Pounds, K. A., Reeves, J. N., King, A. R., et al. 2003, MNRAS, 345, 705
Reid, M. J., Schneps, M. H., Moran, J. M., et al. 1988, ApJ, 330, 809
Ricci, C., Privon, G. C., Pfeifle, R. W., et al. 2021, MNRAS, 506, 5935
Richards, G. T., Kruczek, N. E., Gallagher, S. C., et al. 2011, AJ, 141, 167
Riechers, D. A. 2011, ApJ, 730, 108
Riechers, D. A., Carilli, C. L., Maddalena, R. J., et al. 2011, ApJL, 739, L32
Riechers, D. A., Carilli, L. C., Walter, F., et al. 2011, ApJL, 733, L11
Rybak, M., Hodge, J. A., Vegetti, S., et al. 2020, MNRAS, 494, 5542
Sanders, D. B., Soifer, B. T., Elias, J. H., et al. 1988, ApJ, 325, 74
Sargent, M. T., Daddi, E., Béthermin, M., et al. 2014, ApJ, 793, 19
Schindler, J.-T., Farina, E. P., Bañados, E., et al. 2020, ApJ, 905, 51
Schneider, D. P., Richards, G. T., Hall, P. B., et al. 2010, AJ, 139, 2360
Schneider, R., Bianchi, S., Valiante, R., et al. 2015, A&A, 579, A60
Scoville, N., & Norman, C. 1995, ApJ, 451, 510
Shen, Y., Richards, G. T., Strauss, M. A., et al. 2011, ApJS, 194, 45
Solomon, P. M., Downes, D., Radford, S. J. E., et al. 1997, ApJ, 478, 144
Swinbank, A. M., Lacey, C. G., Smail, I., et al. 2008, MNRAS, 391, 420
Tacconi, L. J., Genzel, R., & Sternberg, A. 2020, ARA&A, 58, 157
Tacconi, L. J., Neri, R., Chapman, S. C., et al. 2006, ApJ, 640, 228
Timmons, N., Cooray, A., Riechers, D. A., et al. 2016, ApJ, 829, 21
Tombesi, F., Cappi, M., Reeves, J. N., et al. 2012, MNRAS, 422, L1
Trakhtenbrot, B., Lira, P., Netzer, H., et al. 2017, ApJ, 836, 8
Vayner, A., Wright, S. A., Murray, N., et al. 2017, ApJ, 851, 126
Vayner, A., Zakamska, N., Wright, S. A., et al. 2021, ApJ, 923, 59
Vieira, J. D., Crawford, T. M., Switzer, E. R., et al. 2010, ApJ, 719, 763
Viero, M. P., Asboth, V., Roseboom, I. G., et al. 2014, ApJS, 210, 22
Vietri, G., Mainieri, V., Kakkad, D., et al. 2020, A&A, 644, A175
Vietri, G., Piconcelli, E., Bischetti, M., et al. 2018, A&A, 617, A81
Walter, F., Carilli, C., Bertoldi, F., et al. 2004, ApJL, 615, L17
Wang, R., Carilli, C. L., Neri, R., et al. 2010, ApJ, 714, 699
Wardlow, J. L., Cooray, A., De Bernardis, F., et al. 2013, ApJ, 762, 59
Weymann, R. J., Morris, S. L., Foltz, C. B., et al. 1991, ApJ, 373, 23
Wright, E. L., Eisenhardt, P. R. M., Mainzer, A. K., et al. 2010, AJ, 140, 1868
Yang, C., Omont, A., Beelen, A., et al. 2017, A&A, 608, A144
Yang, G., Boquien, M., Brandt, W. N., et al. 2022, ApJ, 927, 192
Zavala, J. A., Yun, M. S., Aretxaga, I., et al. 2015, MNRAS, 452, 1140
Zhang, Z.-Y., Ivison, R. J., George, R. D., et al. 2018, MNRAS, 481, 59